

Full-f gyrokinetic particle simulation of centrally heated global ITG turbulence from magnetic axis to edge pedestal top in a realistic tokamak geometry

To cite this article: S. Ku *et al* 2009 *Nucl. Fusion* **49** 115021

View the [article online](#) for updates and enhancements.

Related content

- [Topical Review](#)
X. Garbet, Y. Idomura, L. Villard *et al.*
- [Plasma size and collisionality scaling of ion-temperature-gradient-driven turbulence](#)
Motoki Nakata and Yasuhiro Idomura
- [Study of ion turbulent transport and profile formation](#)
Y. Idomura, H. Urano, N. Aiba *et al.*

Recent citations

- [Efficient Multibyte Floating Point Data Formats Using Vectorization](#)
Andrew Anderson *et al*
- [The Microwave-Heated Bumpy Torus: A Concept for Fusion Energy](#)
J. A. Cobble
- [Benchmarking of flux-driven full-F gyrokinetic simulations](#)
Yuuichi Asahi *et al*

Full-f gyrokinetic particle simulation of centrally heated global ITG turbulence from magnetic axis to edge pedestal top in a realistic tokamak geometry

S. Ku¹, C.S. Chang^{1,2} and P.H. Diamond³

¹ Courant Institute of Mathematical Sciences, New York University, NY 10012, USA

² Department of Physics, Korea Advanced Institute of Science and Technology, Daejeon 305-701, Republic of Korea

³ CASS and Department of Physics, University of California, San Diego, La Jolla, CA 92093, USA

E-mail: sku@cims.nyu.edu and cschang@cims.nyu.edu

Received 1 January 2009, accepted for publication 4 September 2009

Published 30 September 2009

Online at stacks.iop.org/NF/49/115021

Abstract

Global electrostatic ITG turbulence physics, together with background dynamics, has been simulated in a realistic tokamak core geometry using XGC1, a full-function 5D gyrokinetic particle code. An adiabatic electron model has been used. Some verification exercises of XGC1 have been presented. The simulation volume extends from the magnetic axis to the pedestal top inside the magnetic separatrix. Central heating is applied, and a number, momentum and energy conserving linearized Monte Carlo Coulomb collision is used. In the turbulent region, the ion temperature gradient profile self-organizes globally around $R/L_T = (Rd \log T/dr = \text{major radius on the magnetic axis/temperature gradient length}) \simeq 6.5\text{--}7$, which is somewhat above the conventional nonlinear criticality of $\simeq 6$. The self-organized ion temperature gradient profile is approximately stiff against variation of heat source magnitude. Results indicate that the relaxation to a self-organized state proceeds in two phases, namely, a transient phase of excessively bursty transport followed by a $1/f$ avalanching phase. The bursty types of behaviour are allowed by the quasi-periodic collapse of local $E \times B$ shearing barriers.

PACS numbers: 52.55.Fa, 52.65.Tt

1. Introduction

In a laboratory plasma without a large scale MHD instability, a turbulent plasma self-organizes to a global profile in which the heat source, the momentum source, the particle source, the turbulence phenomena the neoclassical phenomena, and the background plasma profile are part of the global self-organization feedback loop. Within this self-organizing loop, experimentalists can only control the sources and sinks (to a less degree) if the confinement geometry is given. The rest of the important observables develop as a result. In order to enhance the predictive simulation capability for tokamak plasma performance, including ITER [1], it is desirable to study turbulent and the neoclassical plasma dynamics self-consistently in a full-function (full-f) simulation code with proper sources and sinks. The resulting plasma behaviours

(such as turbulence spectrum, transport and plasma profiles) are to be compared with experimental observations. A few such codes are emerging in the international research community [2–4].

The ion temperature gradient driven (ITG-driven) modes, if driven unstable, are known to drive robust turbulence activity which may dominate tokamak transport phenomena [5, 6]. Moreover, ITG turbulence energy inverse-cascades to form large scale streamers, and also drives Reynolds stresses which influence mean and zonal toroidal and poloidal flows on scales far in excess of ion gyroradius ρ_i .

We report on global electrostatic ITG-driven simulation results from the full-f gyrokinetic particle code XGC1 [7, 8] in a realistic tokamak geometry, which also includes self-consistent mean dynamics of the plasma (excluding the evolution of the mean magnetic flux, current-density and q profile). Evolution

of the mean plasma is driven by both neoclassical and turbulent effects. The present simulation volume extends from the magnetic axis to an edge pedestal top radius at $\psi_N = 0.9$ (where ψ_N is the poloidal magnetic flux ψ normalized to be 0 on the magnetic axis and 1 at the magnetic separatrix) over the whole toroidal angle. A strong heat source is placed around the magnetic axis. While the plasma ions are simulated with full-f marker particles, electron response is assumed to be adiabatic in this study. Neoclassical solutions with full-f electrons and ions have been reported elsewhere [7]. Coulomb collisions are modelled by a well-known particle, momentum and energy conserving linearized Monte Carlo scheme [9–12], which uses delta-f concept by approximating the background field particles as Maxwellian and which has been shown to reproduce neoclassical physics in full-f mode [7, 13, 14]. In this scheme, the conservation property is assured by adjustment of the particle weights. In a full-f simulation, the particle weights are invariant during the time advance process (Vlasov part of the Fokker–Planck equation). However, the particle weights are allowed to change in the collision process. We note here that there are other full-f collision algorithms which demand the conservation by shifting and scaling of the particle velocities [15].

The work presented here is electrostatic and constitutes only a first step towards achieving a desirable predictive capability. A true predictive capability of a plasma discharge requires not only magnetic field fluctuations but also evolution of the plasma current profile and magnetic equilibrium, MHD dynamics and the interaction of the turbulence with the plasma current profile and MHD dynamics (which includes tearing modes, shear Alfvén modes, kinetic ballooning modes, edge localized mode, resistive wall modes, etc).

The aim of this report is to elucidate the dynamics of turbulence and plasma relaxation to a quasi-stationary self-organized state [16, 17] with a heat source [18] in the full-f code XGC1. We identify two stage processes wherein (a) the first stage is a bursty cycle, marked by the development of bursty turbulent heat flux interconnected with collapses of the self-generated $E \times B$ shear. (b) The second stage is more akin to avalanching near a self-organized critical (SOC) state. In this state, the turbulent heat flux shows a $1/f$ type frequency spectrum, except for the geodesic acoustic mode (GAM) activities at high frequency (with the bursty behaviour reduced to obey the $1/f$ spectrum), and the ion temperature profile saturates globally around roughly constant R/L_T values $\simeq 6.5$ – 7 ($\equiv R \, d \log T / dr =$ major radius/temperature gradient length), which is somewhat above the nonlinear stability boundary $R/L_T \simeq 6$ [19]. Settling down of the initial heat bursts into an avalanche state is similar to the recent observation made in [2]. The central heat source region shows different turbulence activity from the source-free region in that the subcritical strong turbulence, the strong $E \times B$ shearing and the strong transport exist without the bursty phenomenon.

A brief description of the full-f XGC1 gyrokinetic code and the several representative verification exercises are given in sections 2 and 3, respectively. The simulation results are presented in section 4, followed by conclusion and discussion in section 5.

2. The full-f gyrokinetic code XGC1

XGC1 is a full-f gyrokinetic particle-in-cell code [7, 8] which can simulate the whole plasma volume including the magnetic axis, the magnetic separatrix and the biased material wall, by reading in a g-eqsk data file generated from the experimental equilibrium reconstruction [20]. XGC1 in its present form is an electrostatic code. Full-f marker ions and adiabatic electrons are used in this study of ITG turbulence. A heat source is placed at the inner radial boundary to induce a heat flux into the simulation region, and a heat sink is sometimes placed at the outer boundary. Heat source (sink) is normally modelled by raising (lowering) the particle energy in the source (sink) region by a small fraction of particle kinetic energy while keeping the pitch angle invariant. A heat source is always necessary to maintain a radial heat flux, but a heat sink is not necessary in a short time simulation since the heat can be allowed to accumulate at the outer boundary, where the temperature is the lowest, with a rise in the local temperature there. A particle, momentum and energy conserving linear Monte Carlo Coulomb collision operator is built into the particle motion, as described in the previous section [9–13]. Monte Carlo neutral particles can also be simulated together in the full-f XGC family codes [13]. In the present short time simulation, however, the neutral particle routine is not used.

Marker particles follow the electrostatic Lagrangian equation of motion which conserves the mass, canonical angular momentum and energy [21–23].

$$\dot{\mathbf{X}} = (1/D)[v_{\parallel} \hat{\mathbf{b}} + (v_{\parallel}^2/B) \nabla B \times \hat{\mathbf{b}} + \{\mathbf{B} \times (\mu \nabla B - \mathbf{E})\}/B^2], \quad (1)$$

$$\dot{v}_{\parallel} = -(1/D)(\mathbf{B} + v_{\parallel} \nabla B \times \hat{\mathbf{b}}) \cdot (\mu \nabla B - \mathbf{E}),$$

$$D = 1 + (v_{\parallel}/B) \hat{\mathbf{b}} \cdot (\nabla \times \hat{\mathbf{b}}),$$

where v_{\parallel} is the speed of the particle parallel to the local magnetic field vector \mathbf{B} , $\hat{\mathbf{b}} = \mathbf{B}/B$, $\mu = v_{\perp}^2/2B$ is the magnetic moment and \mathbf{E} is the gyro-averaged electric field. A particular feature in XGC1 is the use of a cylindrical coordinate system for the particle advance, which allows particle motion in true arbitrary shaped flux surfaces including the magnetic separatrix and the magnetic X-point. In a conventional magnetic flux coordinate system, the equation of motion encounters a mathematical singularity on the magnetic separatrix surface and the error in the particle motion grows rapidly as it approaches the magnetic separatrix.

In order to take advantage of the slowly varying nature of the electric potential (both neoclassical and turbulent) along the magnetic field lines, the electrostatic potential is solved on an approximately field line following mesh as is usually done in conventional turbulence codes. Meshes on all the poloidal plane are identical (axisymmetric). When a mesh node is mapped along the magnetic field line, it meets approximately another mesh node on the adjacent poloidal plane. The mapping is only approximate because the magnetic field lines do not close unless on the mode rational surface. Due to the field line following mesh in the existence of the magnetic X-point, large flux volume expansion along the field lines and arbitrary wall shape, an unstructured triangular mesh system is used in the radial–poloidal plane (and regular in the toroidal direction) at the expense of computing time. The snapshot

particle characteristics are mapped to the cell nodes for electric field calculation from the gyrokinetic Poisson equation (quasi-neutrality equation).

The macroscopic physical quantities associated with the guiding centre particles in a volume ΔV are defined as follows. $f_i, n_i, m_i, q_i \psi$ and χ_i are the distribution function, density, mass, heat flux in ψ space, and thermal conductivity of the guiding centre ions, respectively. Radial particle flux is zero in the present adiabatic electron model. The volume can be defined as a flux shell for a flux-surface-averaged quantities or any local cell for local quantities.

$$\begin{aligned}
 f_i(X, v_{\parallel}, \mu) &= (1/\pi \Delta V) \sum_{X_j \in \Delta V} w_j \delta(X - X_j) \delta(v_{\parallel} - v_{\parallel j}) \delta(\mu - \mu_j), \quad (2) \\
 W &= \sum_{X_j \in \Delta V} w_j, \\
 n_i &= W/\Delta V, \\
 u_{\parallel} &= \sum_{X_j \in \Delta V} v_{\parallel j} w_j / W, \\
 T_i &= \frac{1}{3} \sum_{X_j \in \Delta V} w_j m_i (2B\mu + (v_{\parallel j} - u_{\parallel})^2) / W, \\
 q_{i\psi_N} &= (1/2) \sum_{X_j \in \Delta V} m_i (2B\mu + (v_{\parallel j} - u_{\parallel})^2) w_j \vec{X}_j \cdot \nabla \psi / W, \\
 \chi_i &= q_{i\psi} / \left(|\nabla \psi|^2 \frac{\partial T}{\partial \psi} \right). \quad (3)
 \end{aligned}$$

The following gyrokinetic Poisson equation, or equivalently the quasi-neutrality equation, is solved on the mesh nodes, with the finite $k_{\perp} \rho_i$ correction to the Pade approximation [24–26],

$$-\nabla_{\perp} \cdot \frac{\rho_i^2}{\lambda_{Di}^2} \nabla_{\perp} \Phi = e (1 - \nabla_{\perp} \cdot \rho_i^2 \nabla_{\perp}) (\bar{n}_i - n_e), \quad (4)$$

where ρ_i is the ion gyroradius vector, λ_{Di} is the ion Debye length, the flux-surface-averaged electron density n_e does not respond to the flux-surface-averaged electrostatic potential and \bar{n}_i is the ion guiding centre density at real position \mathbf{x} [27],

$$\bar{n}_i = \frac{1}{2\pi} \int f_i(\mathbf{X}, \mu, u) \delta(\mathbf{X} - \mathbf{x} + \rho_i) d\mathbf{X} d\mu d\alpha,$$

where α is the gyro-phase. In the left-hand side of equation (4), the quantity ρ_i^2/λ_{Di}^2 has radial dependence through the real ion density (= electron density), which is time invariant in the present adiabatic electron model. In the right-hand side, ρ_i^2 is a function of ion temperature which is radial and time dependent. The above gyrokinetic Poisson equations are valid for steep gradient plasma, too, as long as the plasma gradient scale length is much greater than the ion gyroradius. In some ITG turbulence simulations, the finite $k_{\perp} \rho_i$ correction term is neglected since the ITG modes are localized to low $k_{\perp} \rho_i$ values [2, 3]. However, when the finite $k_{\perp} \rho_i$ effect becomes important, as in the study of trapped electron modes, this term must be kept [24–26].

A full-f particle simulation solves the $df/dt = C(f) + S$ equation directly in a gyrokinetic form, where C is the collision operator and S is the sources and sinks, by following the

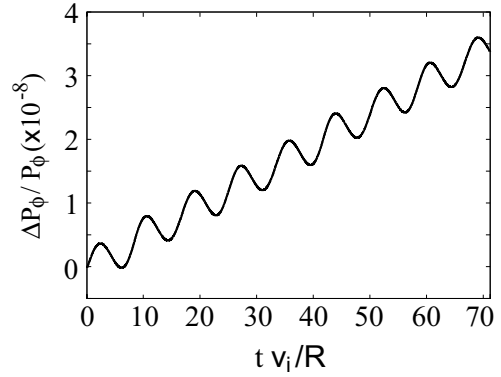


Figure 1. Relative change in canonical angular momentum P_{ϕ} from the error in the 3rd order predictor–corrector solution of the Lagrangian equation of motion is on the order of 10^{-8} over a significant fraction of a typical turbulence simulation period.

guiding centre particle motion (1) in the 5D phase space in the electric field given by equation (4). There is no scale separation in the self-organization between the background and the perturbed plasma dynamics. In return, the simulation is expensive: a full-f gyrokinetic particle-in-cell code requires much more marker particles, roughly by a factor $\sim (n/\delta n)^2$, than a delta-f gyrokinetic code. Fortunately, the simulation can be carried out without suffering from the growth of the random particle weights as in a delta-f code. The disadvantage of the full-f algorithm relative to a delta-f algorithm is thus diminished in a long time simulation (eventually, the weights in delta-f algorithm are bounded). The actual number of full-f marker particles used in this study will be discussed in a later section, together with a discussion on convergence in particle numbers.

3. Basic verification of XGC1

Verification is an important part of the code development. It provides evidence that the equations used in the simulation are solved correctly and accurately. We have performed numerous verification exercises on the basic solving capability of XGC1. The first solving capability we need to check is on the collisionless single particle equation of motion (1) as used in the code, for which the canonical angular momentum conservation is an important barometer since it defines the accuracy in the radial particle position during the simulation (energy conservation is about one order of magnitude more accurate than the canonical angular momentum conservation). Correct momentum conservation sets the basis for correct mean radial potential variation and neoclassical heat flux. Figure 1 shows the change in relative canonical angular momentum $\Delta P_{\phi}/P_{\phi}$ of a 1 keV trapped ion in the 3rd order predictor–corrector time advance of the Lagrangian equation of motion, equation (1), in DIII-D geometry [28]. Each wiggle period represents a banana orbit period ~ 0.1 ms. It can be seen that there is a relative drift of $\Delta P_{\phi}/P_{\phi}$ by about 3×10^{-8} in ~ 7 banana orbit periods, which is a few times shorter than a typical turbulence simulation time in XGC1. Using the small $\Delta\psi_N$ approximation $\Delta\psi_N/\psi \sim \Delta r/a$, the simulation system size $a/\rho_i \sim 200$, where a is the plasma minor radius at the magnetic separatrix surface of DIII-D, and a minimal mean

field radial scale length at $k_r \rho_i \sim 1$ (about 2 cm), the error in the mean potential caused by the erratic drift in the single particle motion in the amount $\Delta P_\phi / P_\phi \sim 3 \times 10^{-8}$ can be easily estimated to be, from equation (4), $\delta_{\text{error}} e\phi / T_i \sim 10^{-5}$ in $\Delta t \sim 7$ banana orbit periods. Thus, it takes about 7000 banana orbit times of 1 keV ion (or ~ 0.7 s) to destroy a physical mean field of $\sim 0.01 T_i$ over $L \sim 2\pi \rho_i$. According to this estimate, the collisionless single particle motions can be considered to be accurate for mean field evaluation over the radial $L \sim 2\pi \rho_i$ (with $\sim 10\%$ mean field level) up to ~ 700 banana bounce periods (~ 70 ms, which is about 30 times longer than the simulation time performed in this work) if we can limit the error in the mean potential to be up to $\sim 1\%$. In the actual simulations presented here, we raised the accuracy even higher by using the 4th order predictor–corrector routine. We note here that the accuracy of the gyrokinetic turbulence simulation, in response to the error in the single particle motion, is significantly raised by the large factor $\rho_i^2 / \lambda_{Di}^2$ arising from the classical polarization response of the ions (the left-hand side of the gyrokinetic Poisson equation (4)). Otherwise, $\Delta P_\phi / P_\phi \sim 3 \times 10^{-8}$ could result in a significant error in the ordinary Poisson equation solution.

The global electrostatic potential solver in XGC1 has been verified using a primitive form of the manufactured solution method in a simple analytic concentric circular cross-sectional toroidal magnetic geometry,

$$\vec{B} = \frac{I}{R} \hat{\phi} + \nabla \psi \times \nabla \phi,$$

$$\psi(r) = B_0 \int_0^r \frac{r'}{q \sqrt{1 - r'^2 / R_0^2}} dr',$$

where $I = B_0 R_0$, $\hat{\phi}$ is the unit vector in the toroidal angle ϕ direction in cylindrical coordinate system, r is the minor radius, R is the major radius, ψ is the poloidal magnetic flux and B_0 and R_0 are the magnetic field strength and major radius on the magnetic axis, respectively. In this procedure, an analytical solution of the gyrokinetic Poisson equation (4) is obtained for a uniform charge distribution in the limit of infinite toroidal aspect ratio $R_0 \rightarrow \infty$ (i.e. the cylindrical limit). The gyrokinetic Poisson equation in XGC1 is solved using the same uniform charge distribution on the right-hand side. The numerical solution obtained from XGC1 is then compared with the analytical solution for a cylindrical equilibrium, checking the convergence as the toroidal aspect ratio is increased. As can be seen in figure 2, the solution from XGC1 rapidly approaches the exact cylindrical solution as R_0 is increased. At $\epsilon = r/R_0 = 0.0895$ the red (XGC1 solution) and black (exact cylindrical analytic) curves are already visually indistinguishable.

The collisional neoclassical equilibrium and ion thermal conductivity have been verified. Figure 3 is a verification of the neoclassical poloidal rotation in full-f mode in a realistic DIII-D geometry (g096333.03337) [28], which is the same shot number as that for the turbulence study in the later section (the safety factor q profile is shown there). The solid line is the radial electric field E_r obtained when we apply the collisionality-dependent analytic formula of Hinton–Hazeltine [29]

$$u_{i,\parallel} = \frac{T_i}{e B_p} \left[k \frac{d \log T_i}{dr} - \frac{d \log p_i}{dr} - \frac{e}{T_i} \frac{d\phi}{dr} \right]$$

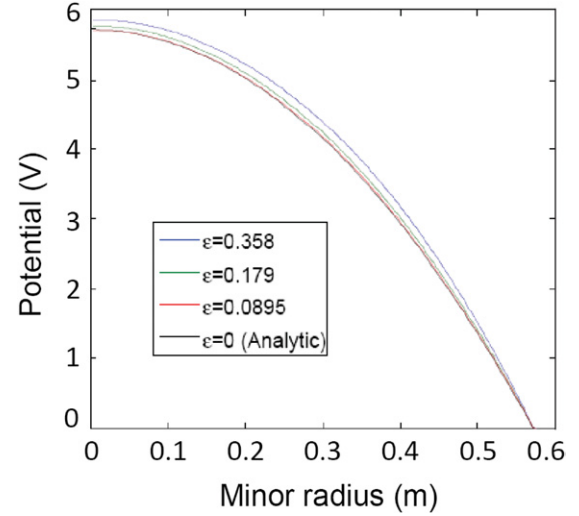


Figure 2. Rapid approaches of the XGC1 solution to the exact cylindrical solution as the inverse aspect ratio is reduced. At $\epsilon = r/R_0 = 0.0895$ the red (XGC1 solution) and black (exact cylindrical analytic) curves are already visually indistinguishable.

to the radial plasma and toroidal rotation profiles from XGC1, and the dashed line is what is actually obtained in XGC1. The collisionality enters into the poloidal rotation factor k . B_p is the poloidal magnetic field strength. Radial profiles of particle density, and initial and final ion temperature are shown together. About 10% level of difference is observed. Considering the approximate nature of the analytic formula, this level of difference is unavoidable in verification. In the neoclassical simulation, the radial temperature (density) varies from 1 keV to 50 eV (5×10^{19} to $1 \times 10^{18} \text{ m}^{-3}$) in the form of a hyperbolic tangent over the normalized poloidal flux from 0.4 to 0.6, with the full radial width of 0.1.

Figure 4 shows the ion thermal conductivity compared with the Chang–Hinton formula [30, 31]. The XGC1 result agrees with the analytic formula within about 15%. Again, considering the approximate nature of the analytic formula, this level of difference is unavoidable in the verification.

The basic turbulence solver capability of XGC1 is verified in delta-f and full-f modes. In figure 5, the dependence of GAM damping rate on the safety factor q is compared with a known analytic theory in delta-f mode [33], as well as other code results (quoted from [32]). A satisfactory result from XGC1 (red diamond) can be seen. Collisionless residual potential agrees well with the analytic result of Hinton and Rosenbluth [34] (see figure 6). In figure 6, the time in the horizontal axis is normalized to the toroidal transit time of a 1 keV ion along the magnetic axis. The linear ITG growth rate and the real frequency from XGC1 in delta-f cyclone plasma (figure 7(a)) is compared against the results from the linear eigenvalue code FULL [35, 36] and the global core gyrokinetic particle code GTC (figure 7(b)) [37] in the global cyclone geometry with $R/L_T = 6.9$. In XGC1, a Gaussian smoothing has been used on the poloidal plane, with the Gaussian width $\simeq 1.5 \rho_i$. The results in figure 7 show reasonably good agreement with the FULL code study and [37], and equally well with other benchmarking studies reported in [19].

Figure 8 shows a comparison of the collisionless delta-f ion thermal conductivity χ_i behaviour in time, between XGC1

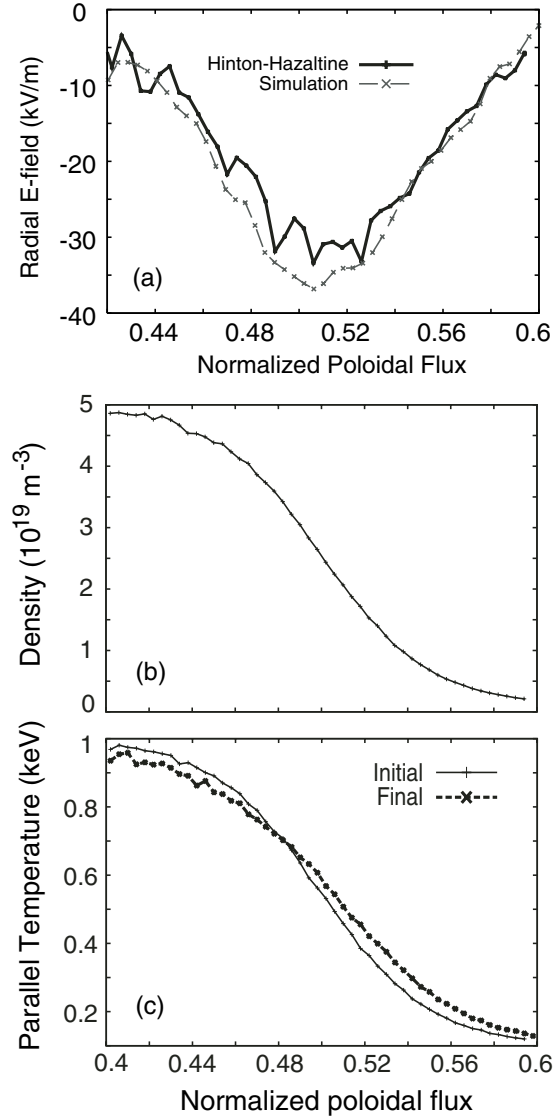


Figure 3. Verification of the neoclassical poloidal rotation in full-f XGC1 in a realistic DIII-D geometry (g096333.03337). (a) The solid line is the radial electric field E_r obtained when we use the collisionality-dependent analytic formula of Hinton–Hazeltine [29] on the radial plasma profiles from XGC1 and the dashed line with X-mark is what is actually obtained in XGC1. Corrugation on the analytic result is from differentiation of the numerical profile data. (b) Radial profile of particle density and (c) radial profile of initial and final ion parallel temperature from the code. The q profile is given in figure 11(b).

in delta-f mode and the delta-f GTC in the global cyclone geometry. The heat source is turned off in the comparison since the two codes use physically different heating methods. Since both codes use Monte Carlo algorithms, two turbulence solutions can only be compared in a statistical sense. The agreement is reasonable. Sourceless χ_i from both codes decays at a later time from the profile relaxation effect.

After the verification of XGC1 in the conventional delta-f turbulence mode [38], the full-f solution is compared with the delta-f solution. For this comparison, we used the full capability delta-f mode, as was used in the comparison performed by Idomura [2], without the

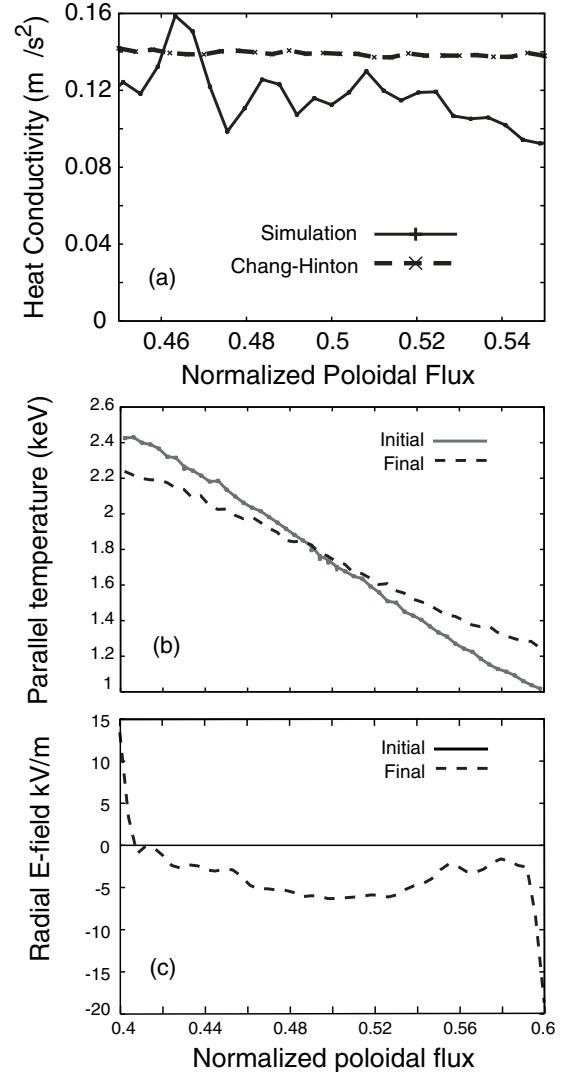


Figure 4. (a) Ion thermal conductivity from XGC1 is compared with the Chang–Hinton formula [30, 31]. (b) The initial and final parallel temperature profiles and (c) radial electric field from the simulation are shown together. Concentric circular flux surface is used for this study with $q = 2$ and a flat density of $5 \times 10^{19} \text{ m}^{-3}$. The radial electric field quickly establishes an ion orbit time and stays steady during the temperature relaxation.

conventional simplification. The heat source and collision are turned off for this comparison. As can be seen in figure 9, the comparison shows reasonable agreement between the delta-f and full-f modes. Both the heat conductivity and the R/L_T show reasonable convergence to each other.

With these verifications ranging from single particle motion, to collisional neoclassical physics and to the GAM and linear/nonlinear ITG physics in delta-f mode, we present the full-f simulation of ITG turbulence in a realistic geometry. We note here that the verification exercises presented here are by no means complete. Continuous verification exercises are to be performed, and new verification methods are under development. There are also a few global full-f turbulence codes being developed in the global fusion community [2–4]. Quantitative comparisons of specific full-f solutions among these codes have not been attempted yet, but to be performed in the near future.

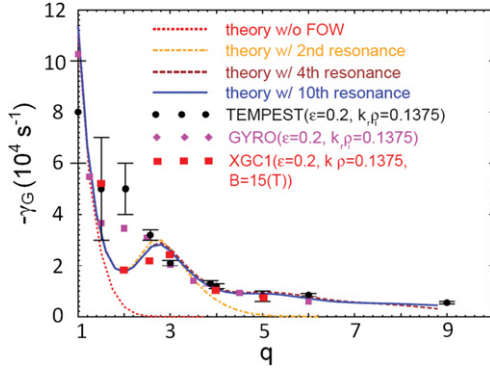


Figure 5. Damping rate γ_0 of GAM versus the safety factor q in comparison with a known analytic theory in delta-f mode (quoted from [32]), demonstrating a satisfactory result from XGC1 (red diamond).

4. Full-f simulation of global ITG turbulence in XGC1

We load the marker particles initially as a local Maxwellian, with flux-function density and temperature profiles. Instead of using the marker particle density to describe the radial profile of plasma number density, we use the particle weight distribution in radius. To be more specific, the particle weight distribution w_j in equation (2) is initialized with ψ_N dependence. This method can resolve the enhanced particle noise problem in the low density region of the plasma profile. We note here that the local Maxwellian loading in the laboratory frame contains some unspecified initial toroidal rotation in an inhomogeneous plasma, which is physically insignificant compared with the other free energy (such as radial pressure gradient). Thus, the effect of initially large toroidal rotation on turbulence cannot be studied in the present simulations. A neutral beam type of external momentum source is not considered in this work either, even though this capability is available in the other XGC family code, XGC0.

We could also initially load the marker particles as a non-local canonical Maxwellian, which may yield more rapid reduction in the initial GAM activities and faster self-organization to neoclassical solution [39], hence an easier growth of turbulence. It is well known that unless the initial GAM activities are subdued, ITG turbulence does not grow in a full-f simulation [40]. However, the canonical Maxwellian loading has a disadvantage in that it is difficult to customize the radial temperature and density profiles. In spite of the obvious disadvantage from the longer initial neoclassical equilibration time, we choose the local Maxwellian loading to take advantage of the easier profile customization. We get compensation for the disadvantage by obtaining a neoclassical radial electric solution in a pre-condition simulation and use it in the turbulence simulation as the initial electric field. Since the initial particle loading is still local Maxwellian, this process does not eliminate the initial GAM oscillations completely, but helps reduce the amplitude and the relaxation time.

The boundary condition we use on the elliptic Poisson equation is that the electrostatic potential on the separatrix surface $\psi_N = 1$ vanishes. Particle simulation volume is bounded by $\psi_N = 0.9$. Any particle leaving the surface $\psi_N = 0.9$ returns to $\psi_N \leq 0.9$ along the collisionless

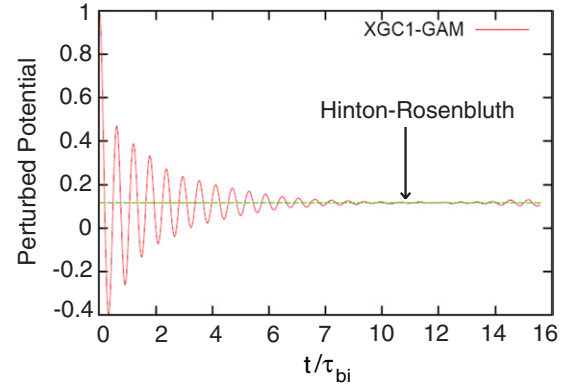


Figure 6. Collisionless residual potential from GAM oscillation in XGC1 agrees well with the analytic result of Hinton and Rosenbluth [34]. Safety factor $q = 1.5$ is used in this study and $\tau_{bi} = 2\pi R/\sqrt{2}v$, where $v = (kT_i/m_i)^{1/2}$.

neoclassical orbit (reflection condition with the proper orbit information). Physical phenomena are studied at $\psi_N \leq 0.8$, away from the reflection boundary.

Initial plasma profiles are shown in figure 10. The initial ion temperature T_i at the magnetic axis is chosen to be 4.5 keV, dropping to 1 keV at the simulation outer edge ($\psi_N = 0.9$, assumed to be near the pedestal top) with linear dependence in the real radius at the outside midplane. The relation between the real distance along the outside midplane and ψ_N is given in figure 11, together with the safety factor q profile. These T_i values are not far off from experimental observations, hence representing a realistic ratio of the ion larmor radius (or turbulence wave length) to the device size ($a_{0.9}/\rho_i \simeq 180$ where $\rho_i \simeq 3$ mm is the average ion gyroradius and $a_{0.9} \simeq 53$ cm is the minor radius at $\psi_N = 0.9$). Of course, the initial T_i profile changes in accordance with the transport as the simulation progresses. For a representative $v_i = (T_i/m_i)^{1/2}$, where m_i is the deuteron mass, we take $T_i = 4$ keV. Note here that the increase in R/L_T with radius indicates that the turbulence drive is stronger at higher minor radius.

Plasma density at the magnetic axis is chosen to be $6 \times 10^{19} \text{ m}^{-3}$, dropping to $4 \times 10^{19} \text{ m}^{-3}$ at $\psi_N = 0.9$ with linear dependence in $\sqrt{\psi_N}$. Since we use adiabatic electrons, the real plasma density profile does not change in time. The temperature and density profiles are within a realistic range of experimental values in DIII-D. However, in order to save computing time, we artificially enhance the collision frequency by a factor of 10 (yielding the average ion collision time to be $\tau_{ic} \simeq 140 v_i/R$). The simulation is then performed to a few to several collision times. Not only the neoclassical relaxations but also the GAM and zonal flow relaxation become faster in proportion to collision frequency. Factor of 10 enhancement of the collision frequency still keeps the plasma in the banana regime even at the simulation outer boundary ($v_* = 0.9$ at $\psi_N = 0.9$), keeping the integrity of the particle orbit dynamics.

Figure 12 shows convergence in marker particle number from the full-f XGC1 test runs in a DIII-D sized circular geometry with the radial heat flux driven by 2 MW of central heating. Ion thermal conductivity χ_i appears to show converged behaviour at a later time for an average 800 particles per grid node. However, R/L_T in figure 12(b)

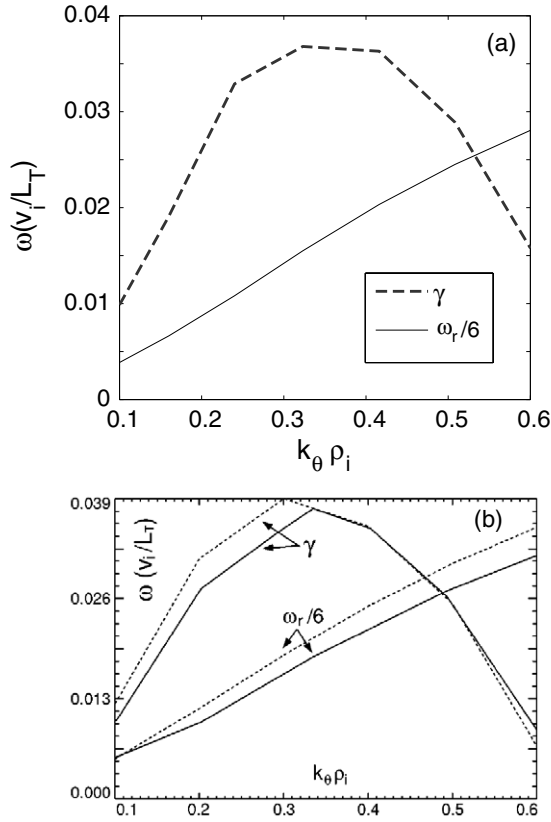


Figure 7. The linear ITG growth rate and the real frequency from (a) XGC1 in delta-f cyclone plasma are compared against the result from (b) the linear eigenvalue code FULL [35, 36] and a gyrokinetic particle code GTC [37] in the global cyclone geometry with $R/L_T = 6.9$. The results shown here compare equally well with other benchmarking studies reported in [19].

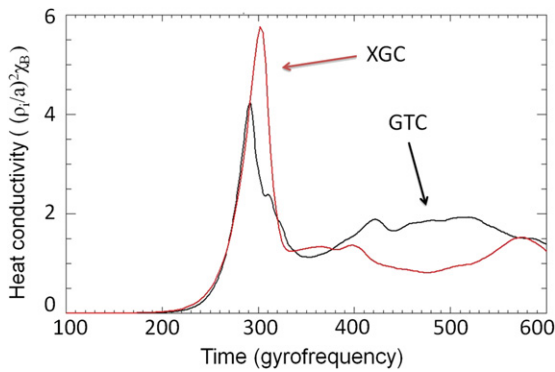


Figure 8. Comparison of the delta-f ion thermal conductivity χ_i behaviour in time, between XGC1 in delta-f mode and the core gyrokinetic particle code GTC in the global cyclone geometry.

shows that 800 particles per node is not enough and that 1600 particles per node is reasonable. Convergence tests in the real simulation geometry show a similar feature. Use of an average ~ 2000 marker particles per grid node (total of 3.1 billion marker particles) is reasonable for the present global ITG turbulence. This yields the noise driven χ_i at the level $\simeq 0.05 \text{ m}^2 \text{ s}^{-1}$, which is identified from a simulation performed without ITG or collisions. In the actual simulation presented here, we raised the particle number to an average

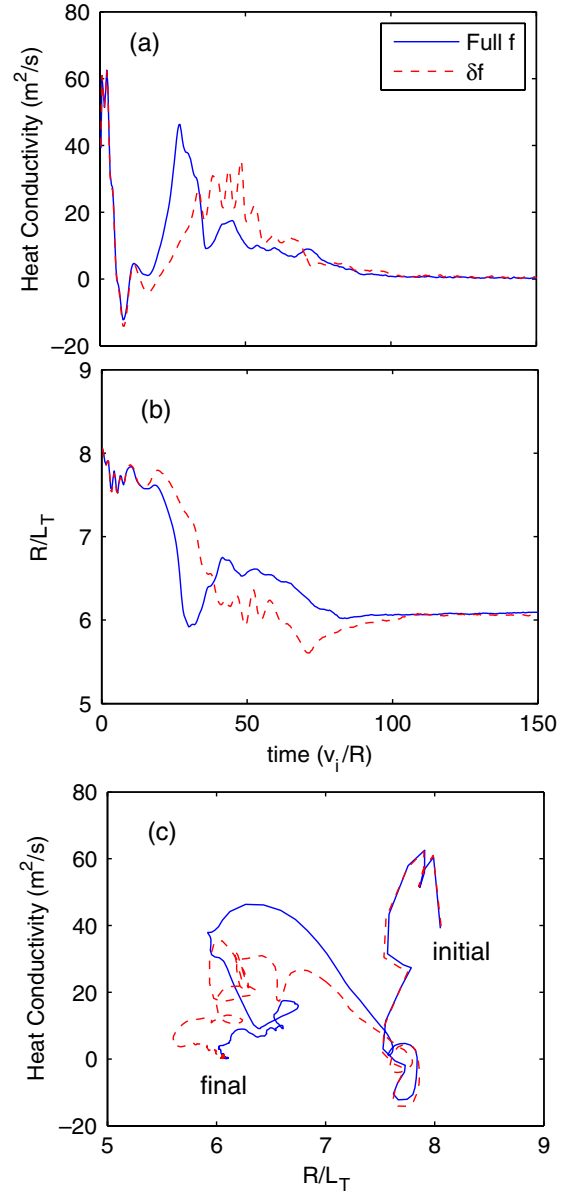


Figure 9. Comparison of XGC1 between the delta-f and full-f modes. (a) Heat conductivity change in time, (b) R/L_T change in time and (c) heat conductivity versus R/L_T are plotted. Both the heat conductivity and the R/L_T show reasonable convergence to each other.

of 3000 per grid node (corresponding to a total of 4.7 billion marker particles. The maximal number of particles used for convergence test was 12 billion particles.). The neoclassical thermal conductivity level $\chi_i \simeq 0.7 \text{ m}^2 \text{ s}^{-1}$ and the combined turbulence-neoclassical thermal conductivity level $\gtrsim 1.5 \text{ m}^2 \text{ s}^{-1}$ from the actual simulations (see pictures later) are much above the noise level. Convergence test in the grid size shows that we need $\simeq 3 \text{ mm}$ average grid size at the outside midplane, which is the average ρ_i and which is what we use in the actual simulations. A simulation takes about 20 h on 59 904 CRAY XT5 cores to reach the self-organized quasi-steady state and another 10 h to confirm that the final state is reasonably out of the initial transient state (total simulation period corresponds to 2.34 ms in real time).

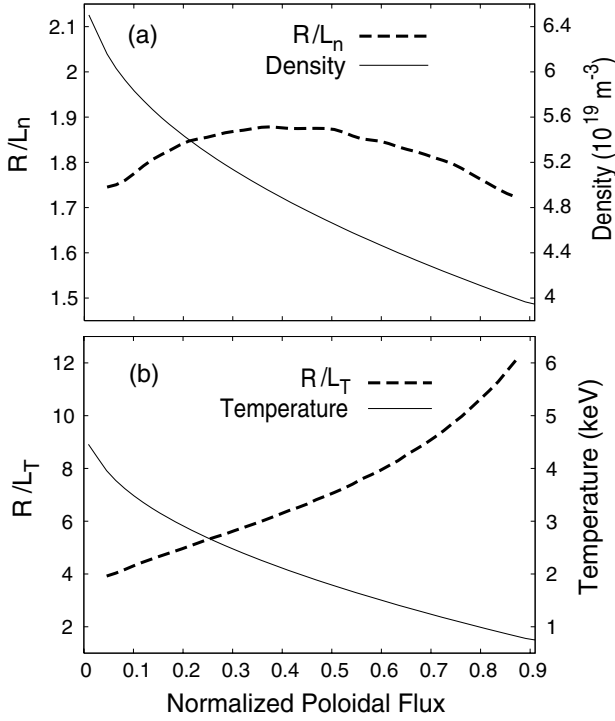


Figure 10. Initial plasma density and temperature profiles. Electron temperature is assumed to be equal to ion temperature. Gradient scale lengths relative to the major radius on the magnetic axis are shown together.

4.5 MW of total heat is added around the magnetic axis ($\psi_N \leq 0.04 \simeq 10 \text{ cm}$) to force a heat flux into the turbulence region. Heating is achieved by raising the particle energy uniformly in the heating region by a small fraction of kinetic energy while keeping the pitch angle invariant. This rate of heating in a small central volume is too large for the local ITG and neoclassical transports to efficiently transport the heat radially outwards. As a matter of fact, the full- f plasma even shows resistance to the local heat flux by developing a strong $E \times B$ shearing rate in the heat source region (relation of this observation to the internal transport barrier formation in a reversed magnetic-shear configuration is to be investigated in the near future). In order to ensure a smooth outward heat flux from the localized heating, we inject a strong local collisional neoclassical transport by further increasing the Coulomb collision rate by another factor of 10 in the central core ($\psi_N \leq 0.08 \simeq 13 \text{ cm}$) somewhat greater than the heat source volume.

An explicit heat sink model is not used in the present simulation. Instead, we use the outer low temperature region as a heat absorption layer and exclude the outer simulation layer ($0.8 < \psi_N \leq 0.9$) from the physics study volume. As a result, the ion temperature gradient around $\psi_N = 0.9$ flattens somewhat in a short time turbulence simulation. We find that this ‘heat absorption layer method’ is adequate to sustain heat flux across the $\psi_N = 0.8$ surface for the duration of the present simulation.

Figure 13 shows the time behaviour of effective ion thermal conductivity (thermal flux divided by local T_i gradient), together with the fluctuating potential squared ($(\delta\Phi)^2$), from the start of the simulation across $\psi_N = 0.45$

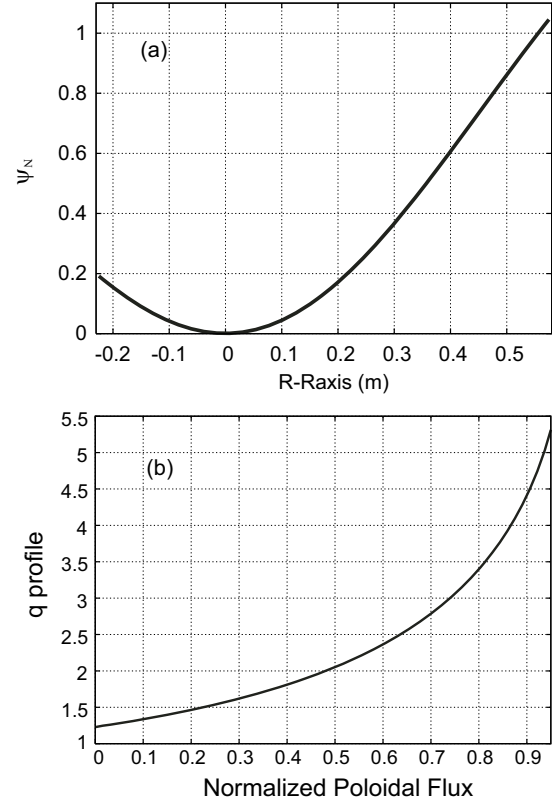


Figure 11. (a) Relationship between the normalized poloidal flux ψ_N and real distance in metres from the magnetic axis (at R_{axis}) to the flux surface (at R) along the midplane. (b) Radial profile of the safety factor q .

which corresponds to $r/a = 0.6$ on the outside midplane with the plasma minor radius ‘ a ’ defined to be the magnetic separatrix surface. The short initial jittering is driven by the GAM oscillations during the toroidal self-organization of the radial electric field, ion distribution function, plasma profile and toroidal rotation in the initial local Maxwellian loading. As the large initial GAMs settle down, ITG modes start to grow at about $75 v_i/R$. As mentioned in the previous section, it is well known that unless the large jittering from the initial GAM activities is subdued, ITG turbulence does not grow in a full- f simulation [40]. The total simulation time is about four times the collision time.

We note here that the initial settling down of the system before the growth of ITG is yet far from the neoclassical equilibrium. The thermal conductivity between 30 and $75 v_i/R$ is greater than the steady-state neoclassical value of the system [30, 31]. Figure 14 is the neoclassical ion thermal conductivity of the system and the total turbulent-neoclassical ion thermal conductivity at the relatively steady final stage.

Figure 13 also shows that there are large multiple bursts of low-frequency heat flux in the initial stage of nonlinear turbulent transport until about $250 v_i/R$, as the initial ion temperature profile and the turbulence begin to self-organize, followed by a relatively steady level of the heat flux behaviour at a later time. The inter-burst period is much greater than the initial GAM jittering period. Since the transient bursty stage shows interesting relation of $E \times B$ shearing dynamics to the radial heat burst, we discuss the bursty and relatively steady

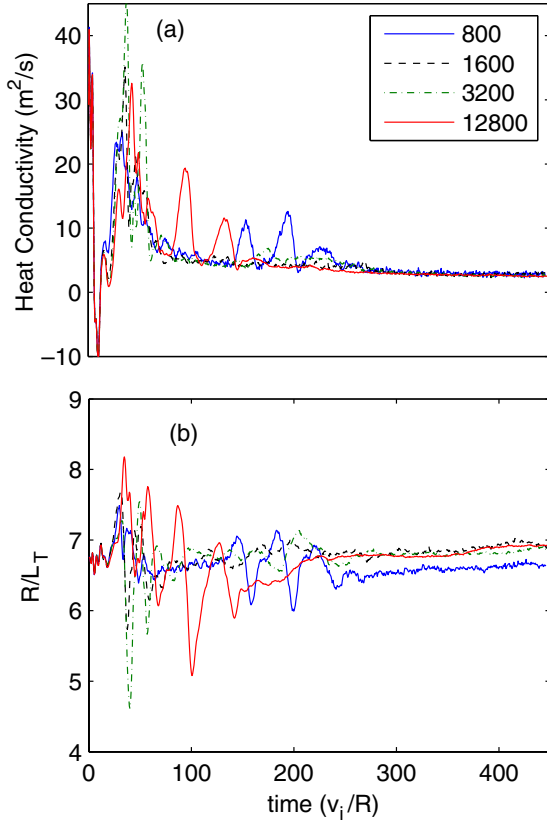


Figure 12. (a) Representative χ_i results from convergence tests in marker particle numbers (average 800, 1600, 3200 and 12800 particles per node). It appears to be that 800 particles per node might be good enough. However, (b) test of R/L_T shows that at least 1600 particles per node is needed.

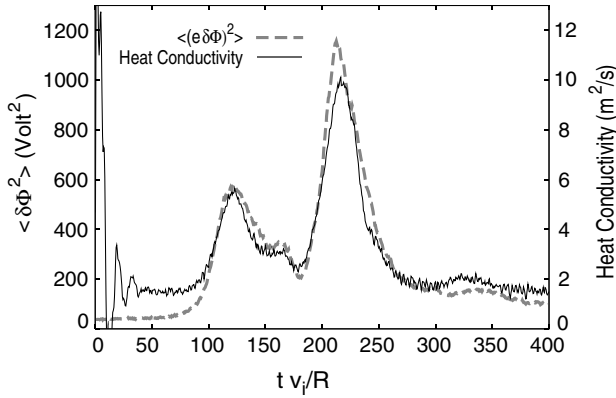


Figure 13. The time behaviour of the effective ion thermal conductivity and the turbulence amplitude squared in MKS unit across the $\psi_N = 0.45$ surface.

stages separately. Figure 15 displays the contour plot of two-dimensional electric potential $\delta\Phi = \Phi - \Phi_{0,0}$ on a constant toroidal angle plane (called poloidal plane) in the bursty stage at $t = 200 R/v_i$.

Figure 16 shows the 2D contour plot of (a) the $E \times B$ shearing rate strength, (b) the radial heat flux strength in the ψ_N -time space and (c) the quasi-steady-state $E \times B$ shearing rate. Simulation lasts for another $200 R/v_i$. Figures 13 and 16 are cut off at $t = 400 R/v_i$ to enhance the visual efficiency

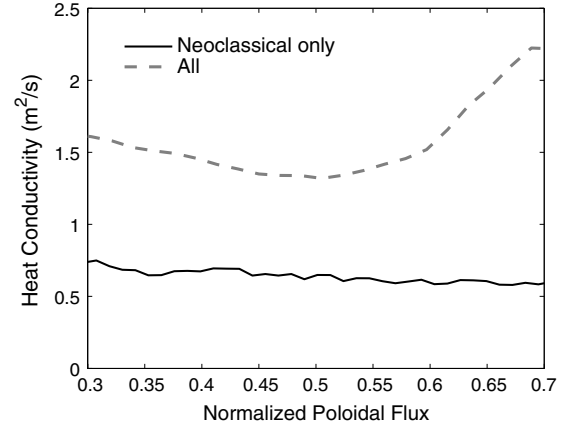


Figure 14. The neoclassical ion thermal conductivity of the system (solid) and the total turbulent-neoclassical ion thermal conductivity (dashed) at the relatively steady final stage.

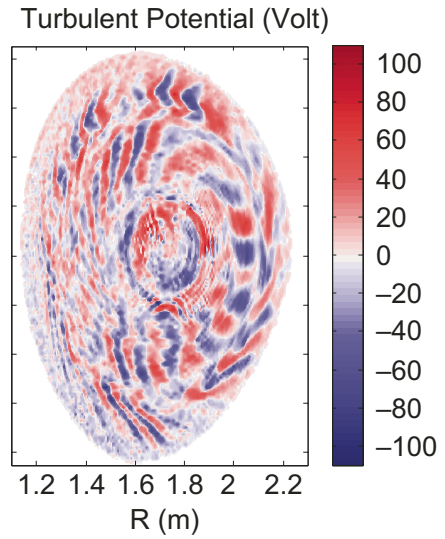


Figure 15. Two-dimensional electric potential contour for $\Phi - \Phi_{0,0}$ on a constant toroidal angle plane in the middle of the bursty nonlinear relaxation stage.

since the quasi-steady does not have much variation. The red colour signifies the high strength region. Radially outward ballistic heat burst contours are marked with dotted ellipses in both figures for visual guide. Ellipses with solid line denote the heat flux during the initial inward propagation of turbulence front from $\psi_N \simeq 0.7$. We see that a radially outward heat burst flows through the openings of the zonal $E \times B$ shearing barriers until the opening narrows. We also see that the $E \times B$ shearing barrier tends to tilt (visually aided by arrows) towards the outward ballistic heat bursts from the vertical zonal flow direction. However, the tilt angle (=radial ballistic speed) of the $E \times B$ shearing is not as strong as the heat flux, indicative of the natural tendency for the $E \times B$ flow to form radial zonal flow structures. This difference eventually leads to destruction of the phase difference between the $E \times B$ shearing and the heat flux, and stops the bursty train.

The radial size of a burst and the inter-burst distance is ~ 5 cm ($\sim 15\rho_i$, where ρ_i is the local gyroradius). After the bursty behaviour is subdued the zonal flows become steady,

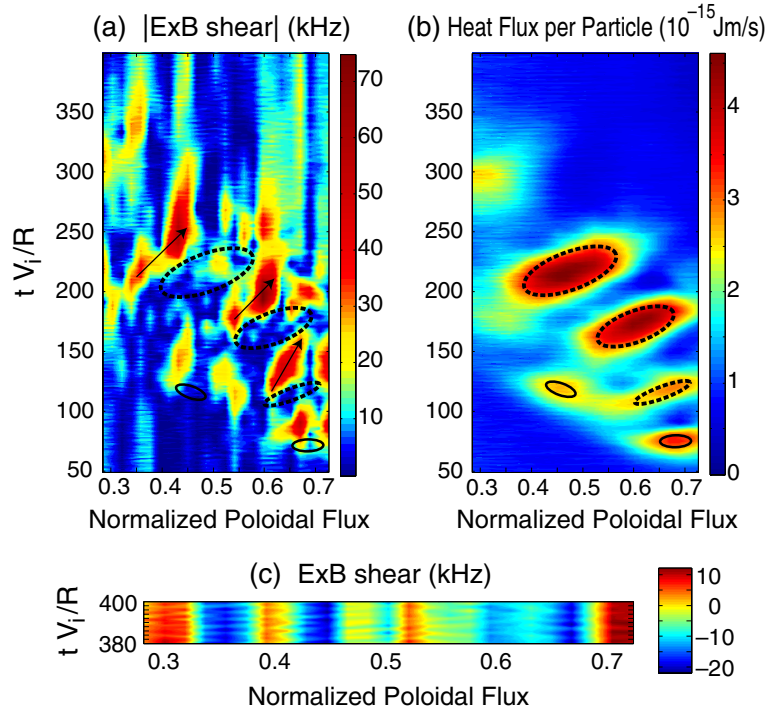


Figure 16. 2D contour plot of (a) $E \times B$ shearing rate strength, (b) bursty heat fluxes and (c) $E \times B$ shearing rate at the beginning of the steady turbulence stage.

as can be seen in figure 16(c), but decaying in collision time scale [34] as will be more clear in figure 17. Figure 17 shows the phase lag and interplay between the heat flux (\propto turbulence intensity) and the $E \times B$ shearing strength at $\psi_N = 0.45$. The decay time of the $E \times B$ shearing is $\sim 50R/v_{i,0.45}$ (a few kilohertz), where $v_{i,0.45}$ is the local ion thermal speed at $\psi_N = 0.45$. This decay time is not correlated with GAM frequency or collision time. It is much slower than the GAM oscillation time and faster than the ion collision time. After the first peak in the heat flux decays, the second peak appears after about twice the $E \times B$ shearing decay time. The radial speed of the ballistic motion of heat burst is about $V_r \simeq (1/5)\rho_i v_i/R \simeq (1/30)\rho_i v_i/L_T$, which is either similar to the analytic intensity burst estimates reported in [41] or somewhat smaller [42, 43]. The distinction between the $\rho_i v_i/R$ and $\rho_i v_i/L_T$ scalings in V_r is difficult to determine in the present simulation since R/L_T quickly self-organizes to a roughly fixed value $\simeq 6.5$ –7.

The bursty heat flux, regulated by the zonal $E \times B$ shearing, continues until the resulting temperature profile is roughly consistent with the turbulence (and total transport). The large bursty behaviour stops and the self-organized state is reached and maintained. In the self-organized state, the local $E \times B$ shearing rate (zonal flow) continues to damp [34]. This study does not give answers to the final saturation of the zonal flow in a collisional full- f simulation because the simulation is not carried out long enough for it. This is another area of focused study in the future. The global $E \times B$ shearing rate is maintained by the global E_r profile. This is consistent with the turbulence self-organization with the global mean profile, which is driven by both neoclassical and turbulent physics. The bursty heat flux observation may have some similarity to a previous study reported in the literature [44]. The relation of the present bursty relaxation to the edge localized mode

relaxation of overly steep pedestal pressure gradient and blob formation is an interesting subject to be studied later.

Figure 18 shows the resulting local temperature gradient behaviour in time at three adjacent radial locations. The first group of peaks shows the local rise in T_i at the inner radius side of the inward-propagating turbulence front. This corresponds purely to the inward arrival of turbulence intensity front. Radially outward ballistic motion of temperature gradient is not seen. The second group of peaks corresponds to the large bursty heat fluxes showing the ballistic outward movement of the temperature gradient. The third group of peaks is weaker, followed by the quasi-steady self-organized temperature gradient.

In the central core, the collisional damping of $E \times B$ shearing is offset by the continuous drive from the heat source, and the strong $E \times B$ shearing is maintained (see figure 15). As a result, the bursty heat flux does not appear there. This phenomenon is not well understood. The possible relation of this phenomenon to the transport barrier formation by localized ion heating is another interesting topic to be studied in the future, especially in a reversed-shear magnetic equilibrium.

Figure 19 shows the frequency spectrum of the heat flux in the middle of the simulation radii at $\psi_N = 0.3$ in the bursty stage ($t = 120$ – $300 R/v_i$) and in the approximately steady stage ($t = 400$ – $600 R/v_i$). It can be seen that the approximately steady stage satisfies the avalanche statistics of $1/r$, except the GAM influence between ~ 50 and 100 kHz. The large scale bursty stage is characterized by extra intensity in the low frequency below 5 kHz during the bursty stage. In the avalanche stage the bursty heat flux is now part of the avalanche process. Smaller scale bursts may still show up in a longer simulation within the $1/f$ avalanche statistics. GAM activities are common to the bursty and avalanche phases. It is

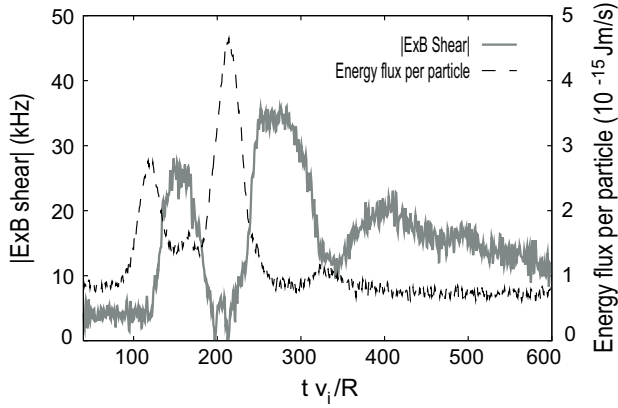


Figure 17. The out-of-phase time behaviour between the heat flux and the $E \times B$ shearing strength at $\psi_N = 0.45$.

our speculation that the heat source driven enhanced turbulence activity in the central core may continuously drive GAMs in the core. An in-depth study is needed for a conclusive insight into the GAM activities in relation to the strong heat flux. The GAM activity is higher at larger minor radii, as can be expected.

Self-organization of the temperature gradient (R/L_T) profile in the turbulent plasma is shown in figure 20(a). The ‘final’ self-organized R/L_T profile stays approximately unchanged around $R/L_T \sim 6.5$ –7 during the turbulence evolution over the whole turbulence radii except in the central core region. The self-organized adjustment of the radial ion temperature itself is shown together in figure 20(b). Since the needed temperature adjustment amount is small, the R/L_T profile is a better barometer of self-organization. In other simulations with heat input as low as 1 MW and as high as 10 MW, the saturation profile of R/L_T is visually indistinguishable in the turbulence region from the 4.5 MW case shown here, suggesting that the self-organized ion temperature profile is ‘stiff’ with respect to the heating strength. What will happen to the stiffness property when the plasma density is also allowed to change is of interest, and is to be investigated in the future when we improve the electron model in XGC1.

The global linear ITG stability boundary in the present magnetic geometry has been investigated by running XGC1 in delta-f mode with the zonal flows turned off. As can be seen from figure 21, the global growth rate becomes negligible at $R/L_T < 4.6$, then approaches marginal stability at $R/L_T = 4$. It can be seen from the figure that the nonlinearly self-organized temperature gradient at $R/L_T \sim 6.5$ is in a strong linear instability regime.

Figure 22 shows the radial variations (shearing) in the mean $E \times B$ flow speed by the turbulence activities. Larger scale $E \times B$ flow speed variations can be seen during the bursty phase, followed by smaller scale variations in the avalanche state.

Figure 23 shows the radial correlation length of (a) $E_{r(0,0)}$ and (b) the turbulent component δE , respectively, during the bursty (100–300 R/v_i) and avalanche (300–400 R/v_i) transport phases. Both axisymmetric and non-axisymmetric turbulence exhibit strong correlation over the distance $\lesssim 1$ cm. The strong correlation distance of δE is shorter than that of $E_{r(0,0)}$ s, as expected. The main difference between them is

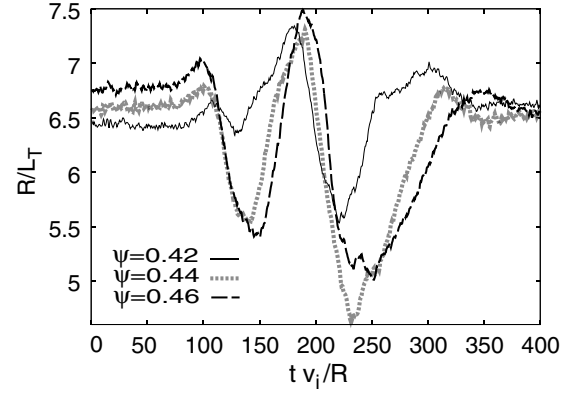


Figure 18. The temperature gradient behaviour in time at three adjacent radial locations.

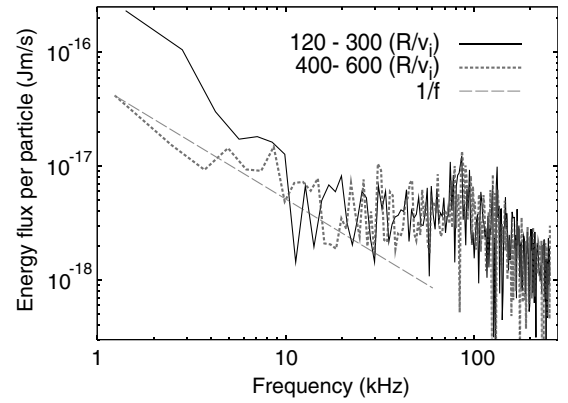


Figure 19. Frequency spectrum of the heat flux in the middle of the simulation radii ($\psi_N = 0.3$) in the bursty stage and in the final quasi-steady state.

in the residual, long range correlation strength. Unlike δE , the axisymmetric modes have a significant residual global correlation, which is not surprising since $E_{r(0,0)}$ in the present full-f simulation contains both the mean and neoclassical component. At the same time, it can be noticed that there are extra long range $E_{r(0,0)}$ correlations in the bursty phase, which is consistent with the time dependent $E \times B$ shearing as discussed for figure 16. On the other hand, δE does not show an obvious sign of this extra correlation in the bursty phase. Detailed study of cross-correlations between the turbulence and heat flux with varying degrees of collisions and axisymmetric zonal/mean flows [45] has not yet been performed.

Energy conservation has been investigated within the volume $0.3 \leq \psi_N \leq 0.7$. In figure 24, total energy flowing into the volume across the inner surface $\psi_N = 0.3$ is shown as a solid black line. The sum of the particle energy change, field energy created and out-flowing energy across the outer surface $\psi_N = 0.7$ is shown as a blue dashed line. The sum of black and blue lines is shown in the red line, which is supposed to trace to zero line in a perfect energy conservation. This simulation shows about 2% error in the total energy conservation. What is to be noticed here is that unlike in a delta-f particle code where the particle weights grow, the energy conservation error in a full-f code should not grow unless numerical errors grow.

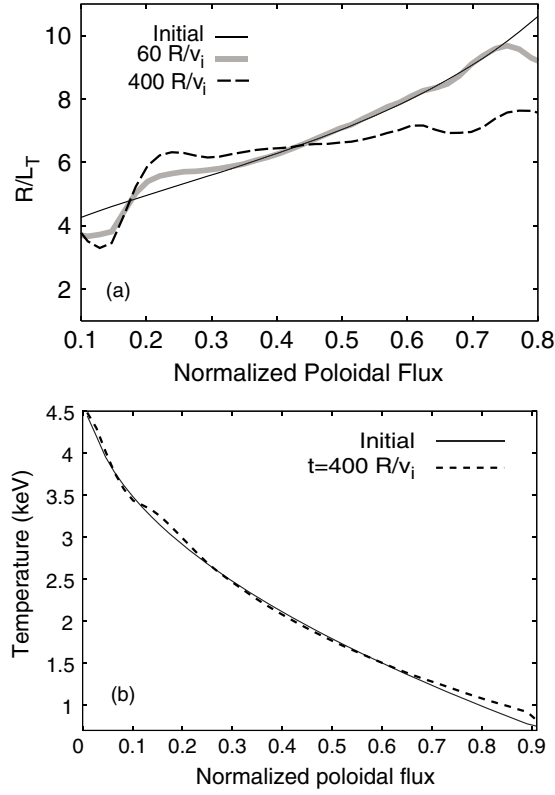


Figure 20. (a) R/L_T profiles are drawn at the initial, after the initial settling down before turbulence, and in the self-organized stage near the end of the simulation. (b) Comparison between the initial and final ion temperature profiles. The self-organized ion temperature profile becomes stiff in variation of heat source strength.

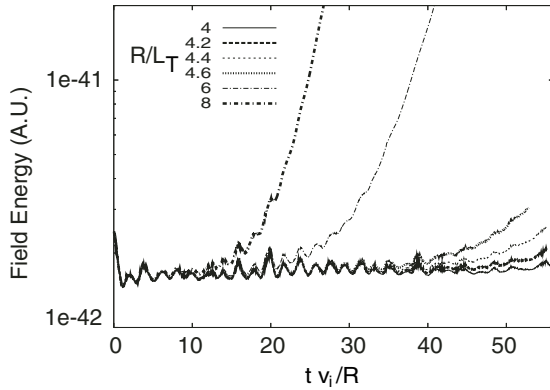


Figure 21. Growth of linear ITG mode for different values of ion temperature gradient R/L_T in the DIII-D geometry. ITG approaches marginal stability at $R/L_T = 4$ and ITG at $R/L_T \sim 6.5$ is strongly unstable linearly.

5. Conclusions and discussions

The XGC1 full-f gyrokinetic code has been used to study the global ITG turbulence from the magnetic axis to edge pedestal top ($\psi_N = 0-0.9$) in a realistic DIII-D magnetic geometry. Electrons are assumed to be adiabatic. Central heating is used to provide radial heat flux in the turbulent transport. A particle number, momentum and energy conserving Monte Carlo collision operator is used to produce proper collision effects in neoclassical and turbulence physics. Collision

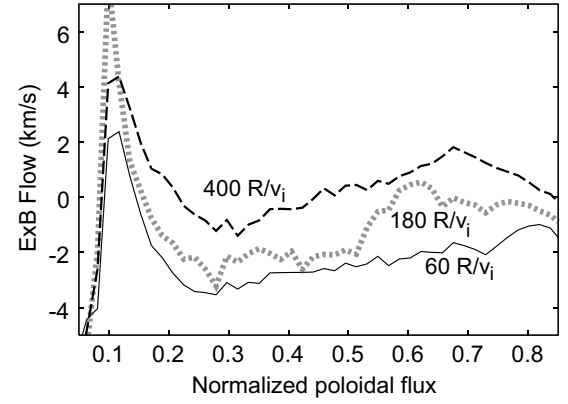


Figure 22. The $E_r \times B$ poloidal rotation speed profile in ψ_N at three different times: after the large amplitude GAM jittering before the turbulence generation ($60 R/v_i$), in the middle of the bursty turbulence phase ($180 R/v_i$) and during the avalanche phase ($400 R/v_i$).

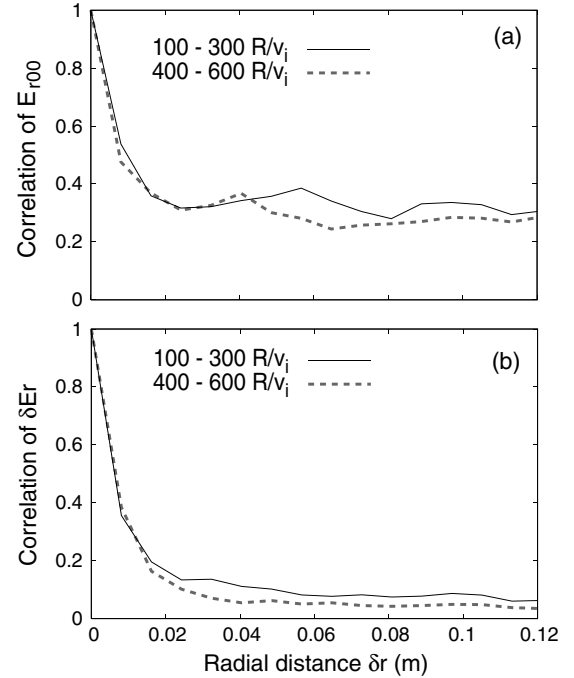


Figure 23. Radial correlation length of (a) $E_{r(0,0)}$ and (b) δE_r turbulence activities during the bursty ($100-300 R/v_i$) and steady ($400-600 R/v_i$) turbulence transport activities.

frequency is artificially enhanced by a factor of 10 to speed up the equilibration and save computing time. XGC1 has been developed to include the magnetic axis, the diverted magnetic field and the material wall geometry, and designed to run on massively parallel high performance computers. Simulations across the magnetic separatrix in DIII-D geometry from $\psi_N \simeq 0.7$ to the material wall have recently been reported elsewhere [8]. The next major goal is a wall-to-wall simulation of the whole plasma to study the core-edge ITG interactions and turbulence spreading.

XGC1 simulation with a strong central heating (4.5 MW within $r \leq 10$ cm) shows that the ion temperature gradient self-organizes around $R/L_T \sim 6.5-7$ in the turbulent region, which is above the linear and nonlinear stability limit. The

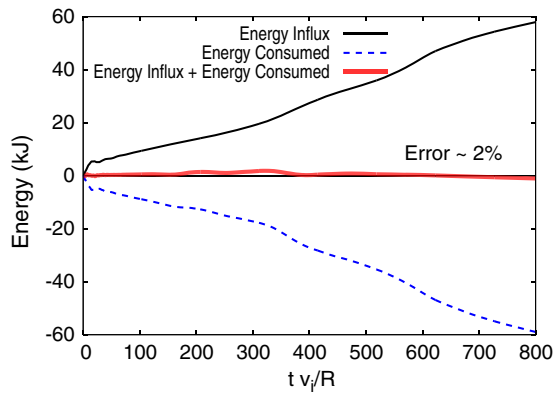


Figure 24. Energy accounting within $0.3 \leq \psi_N \leq 0.7$ between the total influx across the inner boundary (black curve) and the sum of the consumed energy (blue curve) to the particles, the electric field and across the outer boundary. The red line shows the sum of black and blue curves. About 2% error is noticed. Unlike in a delta-f particle code, error in a full-f code does not grow in principle since the particle weights do not grow.

temperature gradient profile shows stiffness to the change in the heating strength at fixed density profile.

The initial plasma profile has radially increasing R/L_T . The initial turbulence front propagates radially inwards, then the turbulence and temperature profile self-organize with each other. During the self-organization of the temperature and turbulence, turbulent heat flux shows a self-regulated quasi-periodic bursty behaviour, during which the turbulence intensity pulses. The self-organizing bursty structure shows ballistic convection radially outwards. A clear correlation between the heat burst and opening up of the $E \times B$ shearing layer has been observed. As the eventual self-organized state settles in, the strong large scale bursty behaviour disappears and the heat flux becomes of the $1/f$ avalanche type. Interaction of ITG turbulence with mean plasma is observed to be not only through η_i evolution but also through the mean $E \times B$ (and possibly toroidal) flow.

For a more complete verification of the full-f XGC1, at least, a comparison with other full-f codes is needed. Such work is in progress and a paper on comparison with the full-f code GYSELA is in preparation (with G. Dif-Pradalier).

We note here that the simulation presented here is electrostatic without particle transport, with fixed magnetic equilibrium and without turbulence interaction with plasma current. Addition of kinetic electrons and electromagnetic effect [46], including tearing modes, to XGC1 turbulence study is the nearest term improvement goal. More experimentally relevant physics effects are to be included later. A routine to evolve magnetic equilibrium and q profile along with the background plasma profile evolution is already incorporated in the sister code and will be used in XGC1. Other routines readily available from XGC0 include toroidal torque source and Monte Carlo neutral transport and recycling. Analytic model magnetic ripple capability is already incorporated into XGC1.

Acknowledgments

The XGC1 full-f gyrokinetic code has been developed collaboratively in the SciDAC FSP Prototype Center for

Plasma Edge Simulation (CPES). The authors wish to express special appreciation to the performance engineering, applied mathematics and data management team members for their invaluable contribution to the XGC1 code development. The authors are grateful to Z. Lin, S. Parker, Y. Chen, T.S. Hahm, Y. Nishimura, W.W. Lee and the CPES Team for their help during the course of XGC1 development. One of the authors (CSC) acknowledges helpful discussions with G. Hammet.

This research has been funded by the US Department of Energy, jointly between the Office of Fusion Energy Science and the Office of Advanced Scientific Computing Research. The computation was made possible through the INCITE award on NCCS Jaguar, ‘Verification and validation of petascale simulation of turbulent transport in fusion plasmas,’ and the ERCAP award at NERSC Franklin, both of which are supported by the US Department of Energy.

References

- [1] Aymar R., Chuyanov V.A., Huguet M., Shimomura Y. 2001 ITER Joint Central Team and ITER Home Teams *Nucl. Fusion* **41** 1301
- [2] Idomura Y., Urano H., Aiba N. and Tokuda S. 2009 *Nucl. Fusion* **49** 065029
- [3] Garbet X. *et al* 2007 *Nucl. Fusion* **47** 1206
- [4] Heikkinen J.A., Henriksson S., Janhunen S., Kiviniemi T.P. and Ogando F. 2006 *Contrib. Plasma Phys.* **46** 490
- [5] Biglari H., Diamond P.H. and Rosenbluth M.N. 1989 *Phys. Fluids B* **1** 109
- [6] Horton W. 1999 *Rev. Mod. Phys.* **71** 735
- [7] Chang C.S. and Ku S. 2008 *Phys. Plasmas* **15** 062510
- [8] Chang C.S., Ku S., Diamond P., Lin Z., Parker S., Hahm T.S. and Samatova N. 2009 *Phys. Plasmas* **16** 056108
- [9] Wang W.X., Nakajima N., Okamoto M. and Murakami S. 1999 *Plasma Phys. Control. Fusion* **41** 1091
- [10] Xu X.Q. and Rosenbluth M.N. 1991 *Phys. Fluids B* **3** 627
- [11] Dimits A.M. and Cohen B.I. 1994 *Phys. Rev. E* **49** 709
- [12] Lin Z., Tang W.M. and Lee W.W. 1995 *Phys. Plasmas* **2** 2975
- [13] Chang C.S. and Ku S. 2004 *Phys. Plasmas* **11** 2649
- [14] Chang C.S. and Ku S. 2006 *Contrib. Plasma Phys.* **46** 496
- [15] Manheimer W.M., Lampe M. and Joyce G. 1977 *J. Comput. Phys.* **138**
- [16] Carreras B.A., Newman D., Lynch V.E. and Diamond P.H. 1996 *Phys. Plasmas* **3** 2903
- [17] Diamond P.H. and Hahm T.S. 1995 *Phys. Plasmas* **2** 3640
- [18] Garbet X., Sarazin Y., Beyer P., Ghendrih P., Waltz R.E., Ottaviani M. and Benkadda S. 1999 *Nucl. Fusion* **39** 2063
- [19] Dimits A.M. *et al* 2000 *Phys. Plasmas* **7** 969
- [20] Lao L.L., St. John H., Stambaugh R.D., Kellman A.G. and Pfeiffer W. 1985 *Nucl. Fusion* **25** 1611
- [21] White R. 1990 *Phys. Fluid B* **2** 845
- [22] Boozer A.H. 1984 *Phys. Fluids* **27** 2441
- [23] Littlejohn R.G. 1985 *Phys. Fluids* **28** 2015
- [24] Nishimura Y., Lin Z., Lewandowski J.L.V. and Ethier S. 2006 *J. Comput. Phys.* **214** 657
- [25] Bottino A., Peeters A.G., Sauter O., Vaclavik J., Villard L. and ASDEX Upgrade Team 2004 *Phys. Plasmas* **11** 198
- [26] Idomura Y., Tokuda S. and Kishimoto Y. 2004 *J. Plasma Fusion Res. Ser.* **6** 17
- [27] Lee W.W. 1983 *Phys. Fluids* **26** 556
- [28] Luxon J.L. 2002 *Nucl. Fusion* **42** 614
- [29] Hinton F.L. and Hazeltine R.D. 1976 *Rev. Mod. Phys.* **48** 239
- [30] Chang C.S. and Hinton F.L. 1982 *Phys. Fluids* **25** 1493
- [31] Chang C.S. and Hinton F.L. 1986 *Phys. Fluids* **29** 3314
- [32] Xu X.Q. *et al* 2009 *Nucl. Fusion* **49** 065023
- [33] Sugama H. and Watanabe T.-H. 2006 *J. Plasma Phys.* **72** 825

- [34] Hinton F.L. and Rosenbluth M.N. 1999 *Plasma Phys. Control. Fusion* **41** A653
- [35] Rewoldt G., Tang W.M. and Chance M.S. 1982 *Phys. Fluids* **25** 480
- [36] Rewoldt G., Tang W.M. and Hastie R.J. 1987 *Phys. Fluids* **30** 807
- [37] Lin Z. and Hahm T.S. 2004 *Phys. Plasmas* **11** 1099
- [38] Lin Z., Hahm T.S., Lee W.W., Tang W.M. and White R.B. 1998 *Science* **281** 1835
- [39] Idomura Y., Tokuda S. and Kishimoto Y. 2003 *Nucl. Fusion* **43** 234
- [40] Dif-Pradalier G., Grandgirard V., Sarazin Y., Garbet X., Ghendrih Ph. and Angelino P. 2008 *Phys. Plasma* **15** 042314
- [41] Hahm T.S., Diamond P.H. and Lin Z. 2005 *Phys. Plasmas* **12** 090903
- [42] Gurcan D., Diamond P.H. and Hahm T.S. 2007 *Phys. Plasmas* **14** 055902
- [43] Garbet X., Sarazin Y., Imbeaux F., Ghendrih P., Gurcan O.D., Bourdelle C. and Diamond P.H. 2007 *Phys. Plasmas* **14** 122305
- [44] Beyer P., Benkadda S., Fuhr-Chaudier G., Garbet X., Ghendrih Ph. and Sarazin Y. 2005 *Phys. Rev. Lett.* **94** 105001
- [45] Diamond P., Itoh S.-I., Itoh K. and Hahm T.S. 2005 *Plasma Phys. Control. Fusion* **47** R35
- [46] Candy J. and Waltz R.E. 2003 *Phys. Rev. Lett.* **91** 045001